

# High-fidelity Hydrodynamic Shape Optimization of a 3-D Hydrofoil

Nitin Garg<sup>a</sup>, Gaetan K. W. Kenway<sup>b</sup>, Zhoujie Lyu<sup>b</sup>, Joaquim R. R. A. Martins<sup>b</sup>, Yin L. Young<sup>a,1</sup>

<sup>a</sup>Department of Naval Architecture and Marine Engineering, University of Michigan, MI 48109, USA

<sup>b</sup>Department of Aerospace Engineering, University of Michigan, MI 48109, USA

---

## Abstract

With recent advances in high performance computing, computational fluid dynamics (CFD) modeling has become an integral part in the engineering analysis and even in the design process of marine vessels and propulsors. In aircraft wing design, CFD has been integrated with numerical optimization and adjoint methods to enable high-fidelity aerodynamic shape optimization with respect to large numbers of design variables. There is a potential to use some of these techniques for maritime applications, but there are new challenges that need to be addressed to realize that potential. This work presents a solution to some of those challenges by developing a CFD-based hydrodynamic shape optimization tool that considers cavitation and a wide range of operating conditions. A previously developed 3-D compressible Reynolds-averaged Navier–Stokes (RANS) solver is extended to solve for nearly incompressible flows, using a low-speed preconditioner. An efficient gradient-based optimizer and the adjoint method are used to carry out the optimization. The modified CFD solver is validated and verified for a tapered NACA 0009 hydrofoil. The need for a large number of design variables is demonstrated by comparing the optimized solution obtained using different number of shape design variables. The results showed that at least 200 design variables are needed to get a converged optimal solution for the hydrofoil considered. The need for a high-fidelity hydrodynamic optimization tool is also demonstrated by comparing RANS-based optimization with Euler-based optimization. The results show that at high lift coefficient ( $C_L$ ) values, the Euler-based optimization leads to a geometry that cannot meet the required lift at the same angle of attack as the original foil due to inability of the Euler solver to predict viscous effects. Single-point optimization studies are conducted for various target  $C_L$  values, and compared with the geometry and performance of the original NACA 0009 hydrofoil, as well as with the results from a multipoint optimization study. A total of 210 design variables are used in the optimization studies. The optimized foil is found to have a much lower negative suction peak, and hence delayed cavitation inception, in addition to higher efficiency, compared to the original foil at the design  $C_L$  value. The results show significantly different optimal geometry for each  $C_L$ , which means an active morphing capability was needed to achieve the best possible performance for all conditions. For the single-point optimization, using the highest  $C_L$  as the design point, the optimized foil yielded the best performance at the design point, but the performance degraded at the off-design  $C_L$  points compared to the multipoint design. In particular, the foil optimized for the highest  $C_L$  showed inferior performance even compared to the original foil at the lowest  $C_L$  condition. On the other hand, the multipoint optimized hydrofoil was found to perform better than the original NACA 0009 hydrofoil over the entire operation profile, where the overall efficiency weighted by the probability of operation at each  $C_L$ , is improved by 14.4%. For the multipoint optimized foil, the geometry remains fixed throughout the operation profile and the overall efficiency was only 1.5% lower than the hypothetical actively morphed foil with the optimal geometry at each  $C_L$ . The new methodology presented herein has the potential to improve the design of hydrodynamic lifting surfaces such as propulsors, hydrofoils, as well as hulls.

**Keywords:** shape optimization, high-fidelity, gradient-based optimization, cavitation, single-point optimization, multipoint optimization, hydrofoil, propulsor.

---

## Nomenclature

$\alpha$	Angle of attack, [°]
$\forall$	Cell volume, [ $m^3$ ]
$\nu_f$	Fluid kinematic viscosity, [ $m^2/s$ ]

---

<sup>1</sup>Corresponding author, email address for correspondence: ylyoung@umich.edu

$\rho_f$	Fluid density, $[kg/m^3]$
$\sigma$	Cavitation number, $\sigma = \frac{P_{ref} - P_{vap}}{0.5\rho_f V^2} [-]$
$\tau_w$	Local wall shear stress, $[N/m^2]$
$A$	Foil planform area, $[m^2]$
$a$	Speed of sound in the fluid, $[m/s]$
10 $c$	Foil chord length, $[m]$
$C_D$	Drag coefficient, $C_D = \frac{D}{0.5\rho_f V^2 A} [-]$
$C_f$	Skin friction coefficient, $C_f = \frac{\tau_w}{0.5\rho_f V^2} [-]$
$C_L$	Lift coefficient, $C_L = \frac{L}{0.5\rho_f V^2 A} [-]$
$C_L/C_D$	Efficiency or lift to drag ratio, $[-]$
$C_p$	Coefficient of pressure, $C_p = \frac{P_{local} - P_{ref}}{0.5\rho_f V^2} [-]$
$D$	Drag force, $[N]$
$L$	Lift force, $[N]$
$M$	Mach number: the ratio between the inflow velocity and the speed of sound, $M = V/a [-]$
$P_{local}$	Local absolute pressure, $[Pa]$
20 $P_{ref}$	Absolute hydrostatic pressure upstream, $[Pa]$
$P_{vap}$	Saturated vapor pressure of the fluid, $[Pa]$
$Re$	Reynolds number: the ratio between the fluid inertial force and fluid viscous force, $Re = Vc/\nu_f [-]$
$t$	Foil thickness, $[m]$
$u_1, u_2, u_3$	Velocity along the $x, y$ and $z$ direction, $[m/s]$
$V$	Inflow velocity, $[m/s]$
<b>S</b>	Vector of state variables in SUMad
CFD	Computational fluid dynamics
FFD	Free-form deformation
RANS	Reynolds-averaged Navier–Stokes

## 30 1. Introduction

In recent years, there has been an increasing interest in developing energy efficient marine propulsors due to increasing fuel prices and desire to reduce the environmental impacts of maritime transportation. The latest amendments to the International Convention for the Prevention of Pollution from Ships (MARPOL) mandates an increasingly stringent Energy Efficiency Design Index (EEDI) score for majority of new vessels. As per the International Council of Clean Transportation (ICCT), the amendments require most new ships to be 10% more efficient beginning in 2015, 20% more efficient by 2020, and 30% more efficient by 2025. Since the propulsor plays a significant role in the system efficiency, there is greater interest in optimization of the propulsor geometry to reduce the net fuel consumption. This work presents a high-fidelity shape optimization tool for hydrodynamic lifting surfaces, capable of handling a large number of design variables and a wide range of operating conditions efficiently.

As noted by Kerwin [1], marine propulsors have complex geometries. Hence, a large number of design variables are required to parametrize their shape. The same is true for other lifting surfaces such as planing vessels, sails, turbines, rudders, hydrofoils, wings, and control surfaces. The hydrodynamic performance of the lifting surfaces is highly sensitive to changes in the surface geometry, particularly at the leading edge, trailing edge, and tip regions. Care is needed in the design to prevent or control laminar to turbulent transition, separation, and cavitation. In particular, cavitation can occur for hydrodynamic lifting surfaces operating at high speeds, near the free surface, or both, which can lead to undesirable effects such as performance decay, erosion, vibration, and noise. Thus, design optimization tools must also be able to enforce constraints to avoid, delay, or control cavitation. Most of the studies carried out so far for hydrofoil or propeller design optimization studies either (1) used potential flow solvers or (2) used Computational Fluid Dynamics (CFD) techniques with a low number of design variables. Thus, there is a need for a high-fidelity CFD-based design optimization tool, capable of handling large number of design variables efficiently to accommodate the complex 3-D geometry and the complex physics of marine propulsors that cannot be captured using Euler or potential flow solvers, such as transition, separation, and stall.

A range of maritime design optimization tools exists in literature. However, as explained earlier, they either used low-fidelity methods, or used high-fidelity methods with low number of design variables. Ching-Yeh Hsin [2] studied two-dimensional (2-D) foil sections using a panel method assuming potential flow. They later performed RANS-based optimization for a 2-D hydrofoil using the Lagrange multiplier method for the optimization of the foil section [3]. Only two design variables were considered: the angle of attack and the camber ratio. Cho et al. [4] carried out an aerodynamic propeller blade shape optimization using a lifting line theory and a 3-D lifting surface theory. They used the twist angle and the chord length as design variables for the lifting line method, and the panel node points as design variables for the 3-D lifting surface method. With optimization, they found a slight increase in efficiency for the SR-7 Propfan blade and the SR-3 Propfan blade. Recently, several authors carried out high-fidelity hydrodynamic shape optimization for naval vehicles and catamarans [5, 6]; they used gradient-free methods, which limited the number of design variables to less than 15 due to the large number of function evaluations compounded with the computational cost of high-fidelity solvers.

The challenge of performing shape optimization with respect to large numbers of design variables using CFD has been tackled in the aircraft wing design through the use of gradient-based algorithms together with efficient methods for computing the required gradients [7, 8, 9, 10, 11]. As an example, Lyu et al. [12] carried out gradient-based aerodynamic shape optimizations based on the RANS equations. They used the adjoint method to compute the gradients and carried out the shape optimization of the Common Research Model (CRM) wing. They minimized the drag coefficient subject to lift, pitching moment, and geometric constraints. The optimization reduced the drag coefficient by 8.5% for a given lift coefficient. They also showed that the 192 design variables provides the best trade-off between the optimized drag value and the number of iterations required for optimization. While this approach has been successfully applied in aircraft wing design, maritime applications bring additional challenges such as higher loading, stronger fluid structure interaction, as well as the potential susceptibility to free-surface, cavitation, and hydroelastic instabilities.

Traditionally, marine propulsors or hydrofoils are designed to achieve optimal performance at a single or only at a few design points, such as, the hump speed, the sustained speed, and the maximum speed. However, depending on the mission objectives, loading conditions, sea states, and wind conditions, a vessel is often required to operate over a wide range of conditions. It is also well known that the performance of some marine propulsors can decay rapidly at off-design points. Nevertheless, many designers still only optimize the propulsor geometry for optimal performance at one design point, and then evaluate the performance at the other critical operating points to ensure satisfactory performance. Such procedure is typically taken because of the high computational cost associated with the multipoint optimization, particularly for complex geometries and with high fidelity methods, but may not yield the global optimal solution. Motley et al. [13] introduced a probabilistic multipoint method to optimize composite marine propellers to minimize the lifetime fuel cost (LFC), while avoiding cavitation and material failure. Kramer et al. [14] used a similar probabilistic multipoint approach to optimize the diameter of a water-jet for maximum overall system efficiency of a surface effect ship (SES). They found a slight increase in lifetime efficiency for the multipoint optimized design compared to the single-point design. Various other researchers (e.g. [15, 16, 17]) also showed that the probabilistic multipoint design can lead to improved performance over the vessel's entire operation profile, instead of at a single design point. However, the above mentioned probabilistic multipoint optimization has been done only with low-fidelity potential flow solvers, primarily due to the high computational cost with high-fidelity methods for multipoint optimization. In this work, using the efficient high-fidelity design optimization tool developed in this paper, the optimal solution from the single-point optimization and the probabilistic multipoint optimization will be

systematically studied.

To avoid performance decay, erosion, vibration, and noise issue when operating at sea, designers should make sure that the propulsors does not only have good efficiency, but also has good cavitation characteristics, for a range of angle of attacks (or lift coefficients). Cavitation is the formation of bubbles in a liquid, which occurs when the local pressure drops to near the saturated vapor pressure, and is a critical driver in marine propulsor design. Brockett [18] presented one of the first studies optimizing hydrofoil performance while considering cavitation. He used a potential theory to determine pressure distribution at an arbitrary lift coefficient for a set incidence angle. He was able to find an optimized cavitation-free hydrofoil for a given design lift coefficient, minimum thickness (based on strength considerations), minimum operation cavitation number ( $\sigma$ ), for an expected range of angle of attacks. Eppler and Shen [19, 20] used a 2-D potential flow-based, inverse wing section design method coupled with turbulent boundary-layer theory to design a series of symmetrical and asymmetrical hydrofoil sections with improved hydrodynamic characteristics in terms of delayed cavitation inception and separation. The width and depth of the minimum pressure cavitation bucket was adapted to practical applications. The depth of the cavitation-bucket, namely, the minimum value of  $-C_p$ , is made as low as necessary to delay the critical cavitation inception speed; the bucket width is made as large as possible to tolerate the fluctuations in the angle of attack or lift coefficient when operating at sea. Kinnas et al. [21] developed an efficient, non-linear boundary element method (BEM) to carry out potential analysis of 2-D and 3-D cavitating hydrofoils. Mishima et al. [22] used the low-order potential-based panel method developed in Kinnas et al. [23]. Mishima et al. [22] carried out a gradient-free optimization to find the optimized foil geometry that minimizes the drag for a given lift and cavitation number, with constraint on maximum cavity length and cavity volume. The influence of viscous effects were considered by applying a constant friction coefficient over the wetted foil surface. Only five design variables were used in their optimization study, and the method is only valid for cases at low to moderate angles of attack due to the potential flow assumption. Zeng et al. [24] developed a design technique using a genetic algorithm to optimize 2-D sections, and used a potential flow-based lifting surface method to incorporate the 2-D section for 3-D propeller blade design.

Given the state-of-the-art just described, most of the previous optimization studies were either based on the potential flow methods, which are not valid for off-design conditions when transition, separation, or stall develops, or based on CFD simulations using very few design variables. Thus, there is a need for an efficient, high-fidelity 3-D design optimization tool that can handle a large number of design variables, enforce constraints to avoid or delay cavitation, and resolve complex viscous, and turbulent flows.

### 1.1. Objectives

The objective of this work is to present an efficient, high-fidelity hydrodynamic shape optimization tool for 3-D lifting surfaces operating in viscous and nearly incompressible fluids, with consideration for cavitation and over a range of operating conditions. An unswept, tapered NACA 0009 hydrofoil is presented as a canonical representation of more complex lifting surfaces like propellers, turbines, rudders, and dynamic positioning devices.

### 1.2. Organization

This section gives a brief overview of layout for the paper. The optimization algorithm is explained in Section 2, with emphasis on the implementation of the low-speed (LS) preconditioner (in Section 2.1) and the development of cavitation constraint (in Section 2.5). Section 3 defines the detailed model setup (Section 3.1), with the convergence behavior, the validation of the implemented LS preconditioner with experimental measurements [25], and the grid convergence study (in Section 3.2, 3.3 and 3.4). Section 3.5 shows the optimization problem setup used to generate the results shown in Section 4. Section 4.1 investigates the influence of number of design variables on the optimal solution. Section 4.2 investigates the difference between the optimal solution obtained using the Euler equations and the RANS equations. Section 4.3 compares the performance of the original NACA 0009 hydrofoil with the single-point optimized solution at various design  $C_L$  points with 210 shape design variables. Section 4.4 compares the performance of the single-point optimized foil with the multipoint optimized foil through a wide range of operating conditions. Conclusions are presented in Section 5 and recommendations for future work are presented in Section 6.

## 2. Methodology

The tool used for optimization is modified from the Multidisciplinary Design Optimization (MDO) of Aircraft Configurations with High-fidelity (MACH) [26, 27]. The MACH framework has the capability of performing static

aeroelastic (aerostructural) optimization that consists of aerodynamic shape optimization and structural optimization. In this work, the MACH framework is extended for hydrodynamic shape optimization of lifting surfaces in viscous and nearly incompressible flows, with consideration for cavitation. While the structural performance is very important, the focus of this work is to present state-of-art hydrodynamic shape optimization. The hydrodynamic optimization tool can be divided into four components: CFD solver, geometric parametrization, mesh perturbation, and optimization algorithm. The formulation of cavitation constraint is described in Section 2.5.

### 2.1. CFD Solver

150 The flow is assumed to be governed by the 3-D compressible Reynolds-averaged Navier–Stokes (RANS) equations without body forces, which can be written as,

$$\frac{\partial \rho_f}{\partial t} + \frac{\partial}{\partial x_j} [\rho_f u_j] = 0 \quad (1)$$

$$\frac{\partial \rho_f u_i}{\partial t} + \frac{\partial}{\partial x_j} [\rho_f u_i u_j + p \delta_{ij} - \tau_{ij}] = 0 \quad (2)$$

$$\frac{\partial E}{\partial t} + \frac{\partial}{\partial x_j} [E u_j + p u_j + q_j - u_i \tau_{ij}] = 0 \quad (3)$$

where  $i, j = 1, 2, 3$ ;  $u_1, u_2$ , and  $u_3$  are the velocity along  $x, y$ , and  $z$  directions, respectively;  $\rho_f$  is the fluid density;  $p$  is the fluid pressure;  $E$  is the fluid energy;  $\tau_{ij}$  is the fluid shear stress tensor;  $\delta_{ij}$  is the Kronecker delta; and  $q_i$  is the fluid heat flux vector. The definition of the coordinates are shown in Figure 1.

160 The CFD solver used in this paper is SUMad [28]. SUMad is a finite-volume, cell centered multiblock solver for the compressible flow equations (shown in Eqs. (1, 2, 3)), and is already coupled with an adjoint solver for optimization studies [29]. The Jameson–Schmidt–Tukel [30] scheme (JST) augmented with artificial dissipation is used for spatial discretization. An explicit multi-stage Runge–Kutta method is used for the temporal discretization. The one-equation Spalart–Allmaras (SA) [31] turbulence model is included in the adjoint formulation.

The focus of this paper is on incompressible flows. Compressible flow equations can be used to solve incompressible flows, where the Mach number ( $M = u/a$ ; where  $u$  is the fluid speed, and  $a$  is the speed of sound in the fluid) is very close to zero, say less than 0.01. However, there are many numerical issues that arise when trying to solve the compressible flow equations at low Mach numbers (in order of 0.01). This is because, at low Mach numbers, there is a large disparity between the acoustic wave speed, i.e.,  $u + a$ , and the waves convection speed, i.e.,  $u$ . In this paper, the low-speed Turkel preconditioner [32] for Euler and RANS equations was implemented, such that the compressible flow solver can be applied to cases with nearly incompressible flows.

170 To make the system well-conditioned, the time derivatives of a flow governing equation are pre-multiplied by a preconditioner matrix,  $\mathbf{D}$ , which slows down the speed of the acoustic waves towards the fluid speed by changing the eigenvalues of the system. The condensed compressible RANS equation (non-conservative form of the equations presented in Eqs. (1, 2, 3)), for the 3-D viscous flows with the preconditioner matrix can be written as,

$$\mathbf{D}^{-1} \mathbf{S}_t + \mathbf{A} \mathbf{S}_x + \mathbf{B} \mathbf{S}_y + \mathbf{C} \mathbf{S}_z = 0 \quad (4)$$

where  $\mathbf{S}_t$  is the time derivative of the state variables;  $\mathbf{S}_x$  (or  $\mathbf{S}_y$  and  $\mathbf{S}_z$ ) is the  $x$  (or  $y$  and  $z$ )-derivative of the state variables; and  $\mathbf{A}$  (or  $\mathbf{B}$  and  $\mathbf{C}$ ) is the flux Jacobian. To accommodate the compressible formulation in SUMad, the preconditioner matrix,  $\mathbf{D}$ , is defined as,

$$\mathbf{D} = \frac{\partial \mathbf{S}_c}{\partial \mathbf{S}_0} \mathbf{D}_0 \frac{\partial \mathbf{S}_0}{\partial \mathbf{S}_c} \quad (5)$$

where  $\mathbf{S}_0 = [p, u, v, w, E]^T$ ;  $\mathbf{S}_c = [\rho_f, \rho_f u, \rho_f v, \rho_f w, \rho_f E]^T$ ; and  $\mathbf{D}_0$  is defined in Eq. (6).

The main property of this preconditioner matrix,  $\mathbf{D}$ , is to reduce the stiffness of the eigenvalues. The acoustic wave speed,  $u + a$ , is replaced by a pseudo-wave speed of the same order of magnitude as the fluid speed. To be efficient, the selected preconditioning should be valid for inviscous computations as well as for viscous computations.

180 There are various low-speed preconditioner available in literature. Some of the most common ones are Turkel [32],

Choi–Merkle [33] and Van leer [34]. A general preconditioner with two free parameters,  $\gamma$  and  $\zeta$ , can be written as,

$$\mathbf{D}_0 = \begin{bmatrix} \frac{\beta M_T^2}{a^2} & 0 & 0 & 0 & 0 & -\frac{\beta M_T^2 \zeta}{a^2} \\ -\frac{\gamma u_1}{\rho_f a^2} & 1 & 0 & 0 & 0 & \frac{\gamma u_1 \zeta}{\rho_f a^2} \\ -\frac{\gamma u_2}{\rho_f a^2} & 0 & 1 & 0 & 0 & \frac{\gamma u_2 \zeta}{\rho_f a^2} \\ -\frac{\gamma u_3}{\rho_f a^2} & 0 & 0 & 1 & 0 & \frac{\gamma u_3 \zeta}{\rho_f a^2} \\ 0 & 0 & 0 & 0 & 1 & 0 \\ 0 & 0 & 0 & 0 & 0 & 1 \end{bmatrix} \quad (6)$$

$$\beta M_T^2 = \min[\max(K_1(u_1^2 + u_2^2 + u_3^2), K_2(u_{1\text{inf}}^2 + u_{2\text{inf}}^2 + u_{3\text{inf}}^2), a^2)] \quad (7)$$

$$K_1 = K_3 \left[ 1 + \frac{(1 - K_1 M_0^2)}{K_1 M_0^4} M^2 \right] \quad (8)$$

If  $\zeta = 1$  and  $\gamma = 0$ , the preconditioner suggested by Choi and Merkle [33] is represented. With  $\zeta = 0$  and  $\gamma = 0$ , the Turkel [32] preconditioner is recovered.

The present method uses  $\gamma = 0$ ,  $\zeta = 0$ . Here,  $a$  is the speed of sound;  $\rho_f$  is the density of the fluid;  $u_{1\text{inf}}, u_{2\text{inf}}, u_{3\text{inf}}$  are the free-stream velocities along  $x$ ,  $y$ , and  $z$ , respectively.  $M$  is the free stream Mach number;  $M_0$  is a constant set by the user to decide the specific Mach number to activate the preconditioner; for  $M > M_0$ ,  $\beta M_T^2 = c^2$ .  $M_0$  is fixed as 0.2 in the current solver, such that the preconditioner is active only when the Mach number is below 0.2.  $K_3$  was set as 1.05 and  $K_2$  as 0.6, which are within the range suggested by Turkel [32]. Note that the preconditioning matrix shown in Eq. (6) becomes singular at  $M = 0$ . Thus, this preconditioner will not work for Mach number very close to 0. The preconditioner was tested for Mach number as low as 0.01. Below that, it runs into some numerical difficulties depending on the problem. Typically, in marine applications, the Mach number ranges from 0.001 to 0.05. The higher end of the range can be easily solved using the modified solver, but numerical issues can be encountered near the lower end. However, in the lower end, the Mach number is so low that there will not be any compressibility effects, and hence the actual solution would be practically the same as the  $M = 0.01$  case.

## 2.2. Geometric Parametrization

The free-form deformation (FFD) volume approach was used to parametrize the geometry [26]. To get a more efficient and compact set of geometric design variables, the FFD volume approach parametrizes the geometric changes rather than the geometry itself. All the geometric changes are performed on the outer boundary of the FFD volume. Any modification of this outer boundary can be used to indirectly modify the embedded objects. Figure 1 displays an example of the FFD control points used for optimization of the tapered NACA 0009 hydrofoil, which will be explained in detail in Section 4.

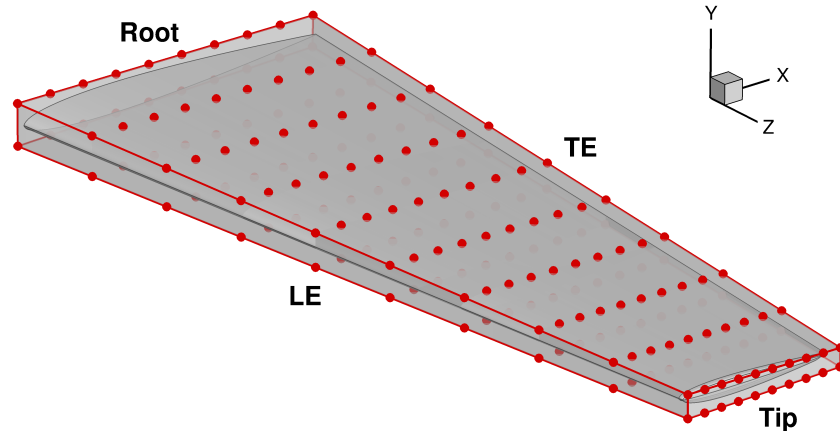


Figure 1: Coordinate system and foil shape design variables using 200 FFD control points (10 spanwise  $\times$  10 chordwise  $\times$  2 thickness), as indicated by the circles.

### 2.3. Mesh Perturbation

As the geometry is modified during the optimization using the FFD volume approach, the mesh must be perturbed to carry out the CFD analysis for the modified geometry. The mesh perturbation scheme is a hybridization of algebraic and linear-elasticity methods [26]. In the hybrid warping scheme, a linear-elasticity-based warping scheme is used for a coarse approximation of the mesh to account for large, low-frequency perturbations; the algebraic warping approach is used to attenuate small, high-frequency perturbations. For the results shown in this paper, the hybrid scheme is not required, and only the algebraic scheme is used because only small mesh perturbations were needed to optimize the geometry.

### 2.4. Optimization Algorithm

The evaluation of the CFD solutions are the most expensive component of hydrodynamic shape optimization algorithms, which can take up to several hours, days or even months. Thus, for large-scale optimization problems, the challenge is to solve the problem to an acceptable level of accuracy with as few CFD evaluations as possible. There are two broad categories of optimization, namely, gradient-free methods and gradient-based methods. Gradient-free methods, such as genetic algorithms (GAs) and particle swarm optimization (PSO), have a higher probability of getting close to the global minima for problems with the multiple local minima. However, gradient-free methods can lead to slower convergence and require larger number of function calls, especially with large number of design variables (of the order of hundreds) [35]. To reduce the number of function evaluations for cases with large number of design variables, gradient-based optimization algorithm should be used. Efficient gradient-based optimization requires accurate and efficient gradient calculations. There are some straight forward algorithms like finite difference; they are neither accurate nor efficient [36]. The complex-step method yields accurate gradients, but are not efficient for large-scale optimization [36, 37]. Thus, for gradient calculations, the adjoint method is used in this paper. The adjoint method is efficient as well as accurate, but is relatively more challenging to implement [29].

The optimization algorithm used in this paper is called SNOPT (sparse nonlinear optimizer) [38]. SNOPT is a gradient-based optimizer that utilizes a sequential quadratic programming method. It is capable of solving large-scale nonlinear optimization problems with thousands of constraints and design variables.

### 2.5. Design Constraint on Cavitation

As explained earlier in section 1, cavitation is one of the most critical aspects of marine propulsors design. Hence, a constraint on the pressure coefficient,  $C_p$  (in Eq. (9)), to avoid the local absolute pressure ( $P_{\text{local}}$ ) reaching the vapor pressure ( $P_{\text{vap}}$ ) on any point on the foil surface, was developed. The cavitation number,  $\sigma$ , is defined in Eq. (10). Cavitation takes place when  $P_{\text{local}} \leq P_{\text{vap}}$ , or  $-C_p \geq \sigma$ , and hence the constraint can be expressed as shown in Eq. (11).  $P_{\text{ref}}$  is the absolute hydrostatic pressure upstream,  $V$  is the relative advance velocity of the body.

$$C_p = \frac{P_{\text{local}} - P_{\text{ref}}}{0.5\rho_f V^2} \quad (9)$$

$$\text{Cavitation number, } \sigma = \frac{P_{\text{ref}} - P_{\text{vap}}}{0.5\rho_f V^2} \quad (10)$$

$$\text{Constraint, } -C_p - \sigma < 0 \quad (11)$$

With change in design variables, the constraint function shown in Eq. (11) for a cell on the foil surface will either be inactive ( $-C_p - \sigma < 0$ ) or active ( $-C_p - \sigma \geq 0$ ), resulting in a step function, which violates the continuously differentiable assumption for gradient-based optimization method. To overcome this issue, a Heaviside function,  $H$ , as shown in Eq. (12), was applied over each cell on the foil surface to make the constraint smooth and continuously differentiable.

$$H(-C_p - \sigma) = \frac{1}{1 + e^{-2k(-C_p - \sigma)}} \quad (12)$$

The smoothing parameter  $k$  of 10 is used to generate the results shown in this paper. The Heaviside function helps in smoothing out the constraint function and also embeds an inherent safety factor in the constraint function.

### 3. Validation and Formulation

#### 3.1. Model Setup

For all the results presented in this paper, an unswept, tapered NACA 0009 hydrofoil was studied with an aspect ratio of 3.33 (a span length of 0.3 m and a mean chord length of 0.09 m, with maximum chord length of 0.12 m at the root and a minimum chord length of 0.06 m at the tip),  $Re = 1.0 \times 10^6$ , and  $M = 0.05$ . The mesh used for all the optimization and validation results is shown in Figure 2. The mesh used is a structured O-grid with 515,520 cells and a  $y^+$  of 1.1. There are approximately 20 elements in the normal direction from the foil surface to encapsulate the boundary layer. The domain size is 30 chord lengths in all the directions.

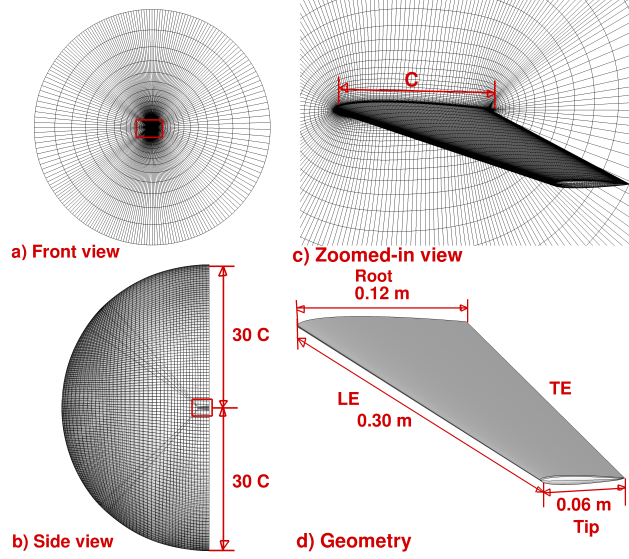


Figure 2: Mesh (515,520 cells) used for the RANS optimization of a tapered NACA 0009 hydrofoil at  $Re = 1 \times 10^6$ . a) Front view of the RANS mesh with the boxed in portion showing the location of the foil. b) Side view of the RANS mesh with boxed in portion showing the location of the foil. c) The zoomed-in view of the foil, showing the mesh near the foil leading edge (LE) and trailing edge (TE). d) Geometry with the dimensions of the tapered NACA 0009 hydrofoil.

#### 3.2. Convergence Behavior of the Low-Speed Preconditioner Solver

As shown in previous literature [32], low-speed preconditioners typically reduces the speed of the system significantly and thus, the convergence speed also reduces. The slow convergence rate makes it difficult to be used for analysis, leave aside optimization. To overcome the slow convergence issue, the spectral radius method used to calculate the time step size in the Runge–Kutta 4<sup>th</sup> order (RK4) solver, was modified to reflect the state variables after preconditioning. The spectral radius,  $r$ , of a matrix can be defined as the maximum absolute value of its eigenvalues ( $\lambda_i$ ), as shown in Eq. (13). The modified time step size is calculated by finding the spectral radius of the preconditioned flux Jacobians,  $\mathbf{A}$ ,  $\mathbf{B}$ , and  $\mathbf{C}$ , as shown in Eq.(14).

$$r(\mathbf{A}) = \max|\lambda_i| \quad (13)$$

$$\Delta t = CFL \times \forall \times \frac{1}{r(\mathbf{A}) + r(\mathbf{B}) + r(\mathbf{C})} \quad (14)$$

where  $|\lambda_i|$  are the eigenvalues of the respective matrices.  $r(\mathbf{A})$  represents the spectral radius of  $\mathbf{A}$ , and similarly for  $r(\mathbf{B})$  and  $r(\mathbf{C})$ .  $CFL$  is the CFL number and  $\forall$  is the volume of the particular cell.

Table 1 shows the comparison of the time and iterations taken by SUMad at a Mach number of 0.8, and the Low-Speed SUMad (LS SUMad) at a Mach number of 0.05. All the simulations were carried out for a tapered NACA 0009 hydrofoil (as shown in section 3.1) by solving the RANS equations, at  $Re = 1 \times 10^6$  and angle of attack ( $\alpha$ ) of  $6^\circ$ . The CPU time and number of iterations required for convergence for the two cases are compared in Table 1. Both simulations used a 515,520 cell mesh (shown in Figure 2) with a  $y^+$  of 1.1. All the solutions were converged



until the residuals were less than  $1 \times 10^{-6}$ . The simulations were carried out with 64 processors (2.80 GHz Intel Xeon E5-2680V2 processors) on 4 cores at the University of Michigan High Performance Computing (HPC) flux cluster. As observed from Table 1, the LS SUMad takes approximately 2.2 times the CPU time taken by the original SUMad, which is acceptable to carry out optimization studies.

Table 1: Comparative study of the CPU time and the number of iterations required for convergence for the RANS-simulation results using the original SUMad (for  $M = 0.8$ ) and the LS SUMad (for  $M = 0.05$ ) for a tapered NACA 0009 hydrofoil at  $Re = 1.0 \times 10^6$  and angle of attack ( $\alpha$ ) of  $6^\circ$ .

Equations	SUMad at M=0.8	LS SUMad at M=0.05
Time (s)	343	743
No. of Iterations	2559	6144

### 3.3. Accuracy of the LS SUMad

To validate the CFD prediction with the low-speed preconditioner, a 3-D tapered NACA 0009 hydrofoil (as shown in section 3.1), with  $Re = 1.0 \times 10^6$  and  $M = 0.05$  was studied. The predictions were compared with experimental measurements conducted at the Cavitation Research Laboratory (CRL) variable pressure water tunnel at the University of Tasmania [25]. The operating velocity and pressure range in the tunnel was of 2 - 12 m/s and 4 - 400 kPa, respectively. The tunnel test section is 0.6 m square by 2.6 m long. They tested on four foils of similar geometry but with different materials, namely, SS (stainless steel-316L), Al (Aluminum-6061T6), CFRP-00, and CFRP-30 (CFRP are composites where the number denotes the alignment of unidirectional fibers). The geometry dimensions were selected such that confinement effects are negligible. They reported estimated uncertainty of less than 0.5% in the force measurement and uncertainty in  $\alpha$  of less than  $0.001^\circ$ .

Table 2 shows the comparison of the parameters used in the experiment and in the numerical solution. All the parameters were matched (including the Reynolds number), except for the Mach number. However, as the compressibility effects are almost negligible for Mach number less than 0.1, this discrepancy in Mach number should not affect the solution. To get the Mach number of 0.05 for the same Reynolds number, the constants were modified in the Sutherland's law to change the speed of sound while maintaining the fluid density as measured in the experiments.

A 515,520 cell mesh, as shown in Figure 2, was used for the RANS solution with a  $y^+$  of 1.1. To validate the LS SUMad solver, the results were compared to experimental results of  $C_L$  and  $C_D$  for the SS foil from [25] at  $Re = 1.0 \times 10^6$ . As can be observed from Figure 3, there is a good agreement between the predicted and measured lift coefficient ( $C_L$ ) and drag coefficient ( $C_D$ ) values for a wide range of angles of attack. The LS SUMad (with the SA turbulence model), over predicts the  $C_D$  value by 14.37%, and under-predicts the  $C_L$  value by 3.3%, at  $\alpha = 6^\circ$ , when compared with the experimental results [25]. Results were also compared with solution from the commercial CFD software (ANSYS) with a 21.3 million element mesh at an  $\alpha = 6^\circ$  (displayed as an open black diamond in Figure 3), using the URANS (unsteady RANS) method with the k-omega shear stress transport ( $k - \omega$  SST) turbulence model. The difference was 2.9% in  $C_L$  and 1.7% in  $C_D$  at  $\alpha = 6^\circ$  between the LS SUMad and CFX predictions, in spite of the different turbulence models. For  $Re = 1.0 \times 10^6$ , experiments were only conducted until a maximum angle of attack of  $6^\circ$ , to avoid excessive forces on the foil.

Table 2: Problem setup for RANS validation of the modified LS SUMad solver for an unswept tapered NACA 0009 hydrofoil with the experimental results from [25]. The RANS mesh is shown in Figure 2.

Parameter	Experiment [25]	LS SUMad
Geometry	NACA 0009	NACA 0009
Aspect ratio	3.33	3.33
Reynolds number	$1 \times 10^6$	$1 \times 10^6$
Mach number	0.008	0.05

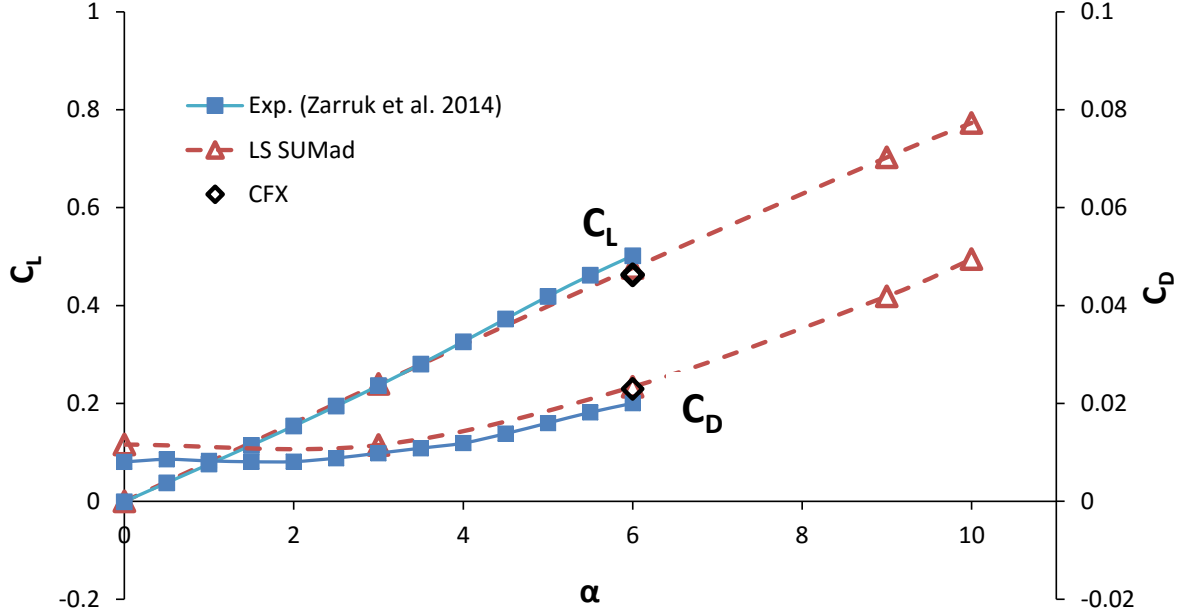


Figure 3: Comparison between the predicted lift coefficient ( $C_L$ ) and drag coefficient ( $C_D$ ) values at various angle of attack ( $\alpha$ ) obtained using LS SUMad with the experimental measurements from [25] for a tapered NACA 0009 hydrofoil. The key parameters for the foil are shown in Table 2 and the mesh with 515,520 cells ( $y^+ = 1.1$ ) for LS SUMad is shown in Figure 2. The conditions selected corresponds to an unswept Stainless Steel (SS) tapered NACA 0009 hydrofoil at  $Re = 1.0 \times 10^6$  for  $M = 0.05$ , reported in Table 2. The SA turbulence model is used for the LS SUMad RANS simulations. The open black diamond symbols represent the solution from the commercial CFD solver, ANSYS, with the k- $\omega$  SST model with a 21.3 million cell mesh ( $y^+ \approx 1.0$ ).

### 3.4. CFD Grid Convergence Study

To ensure that the results are independent of the mesh size, the grid convergence was studied with three different mesh sizes: 515,520 cells, 4,124,160 cells, and 32,993,280 cells for the 3-D tapered NACA 0009 hydrofoil (as shown in section 3.1), with  $Re = 1.0 \times 10^6$ ,  $M = 0.05$ , and  $\alpha = 6^\circ$ . As shown in Table 3, there is a difference of 0.19% in  $C_L$  values and 2.63% in  $C_D$  values for the coarsest mesh and the finest mesh. Figure 4 shows the comparison of  $C_p$  variation along the chordwise direction for the three meshes at mid-span position ( $Z/S = 0.50$ ), and they all seem to lie on top of each other with only slight difference near the leading edge. Thus, to save on the computational cost, the mesh size of 515, 520 cells was used for the optimization study shown in the next section.

Table 3: Comparison of  $y^+$ ,  $C_L$ , and  $C_D$  values from RANS-simulation for the tapered NACA 0009 hydrofoil at  $Re = 1.0 \times 10^6$ ,  $M = 0.05$ , and  $\alpha = 6^\circ$  using different mesh sizes with the LS SUMad solver.

Mesh Size	$y^+$	$C_L$	$C_D$
515520	1.1	0.4767	0.0234
4124160	0.8	0.4753	0.0233
32993280	0.5	0.4758	0.0228

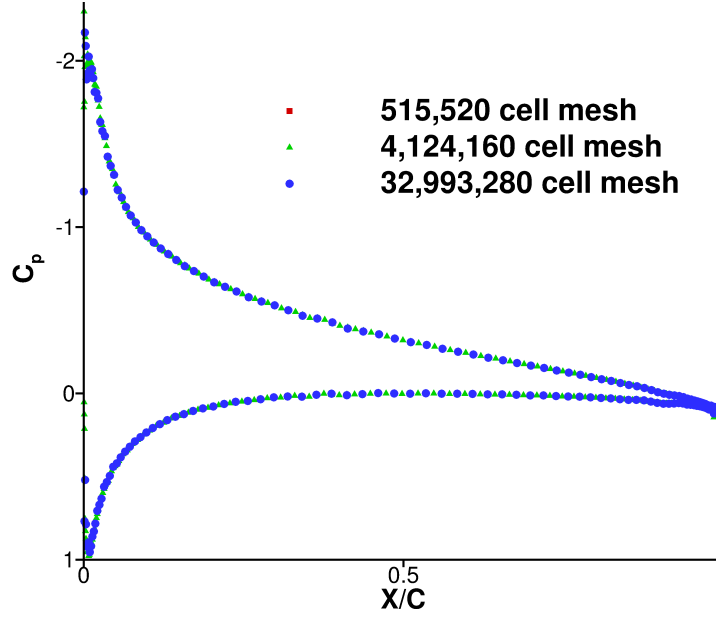


Figure 4:  $C_p$  variations along the chord for the three different meshes is displayed at mid-span ( $Z/S = 0.50$ ) location. The RANS-simulations were carried out using the LS SUMad solver for the tapered NACA 0009 hydrofoil at  $Re = 1.0 \times 10^6$ ,  $M = 0.05$  for  $\alpha = 6^\circ$ . They all lie on top of each other with only slight difference at the leading edge.

### 3.5. Optimization Problem Formulation

To demonstrate the advantages of hydrodynamic shape optimization, the optimization was carried out for the 3-D tapered NACA 0009 hydrofoil (as shown in section 3.1), with  $Re = 1.0 \times 10^6$  and  $M = 0.05$ . The optimization problem setup is described in Table 4. The drag coefficient,  $C_D$ , is minimized for a given  $C_L$  and a given cavitation number,  $\sigma$  (as defined in Eq. 10), for the results shown in Section 4. Constraint on the minimum volume and minimum thickness are also detailed in Table 4.  $C_L^*$  is the target  $C_L$ ,  $\forall$  is the volume of the optimized foil,  $\forall_{base}$  is the volume of the original foil,  $t_{base}$  is the thickness of the original foil at a given section. The leading edge of the hydrofoil is also constrained to deform to prevent any random behavior at the leading edge.

Figure 2 shows the mesh used for the RANS based optimization, with an approximately 515,520 cells. Figure 1 depicts the FFD volume used for optimization.

Table 4: Optimization problem for a tapered NACA 0009 hydrofoil.

	Function variables	Description	Qty.
minimize	$C_D$	Drag coefficient	1
Design variables	$f$	FFD control points	200
		Twist design variables	10
Constraint	$C_L = C_L^*$	Lift coefficient constraint	1
	$t_i \geq 0.8 \times t_{base}$	Minimum thickness constraint	400
	$\forall \geq \forall_{base}$	Minimum volume constraint	1
		Fixed leading edge constraint	10
	$-C_p < \sigma = 1.6$	Cavitation number	1

The angle of attack is defined by the original global geometry coordinates with respect to the inflow, which does not change over the course of optimization, unless the angle of attack is one of the design variables. Table 5 shows the angle of attack ( $\alpha$ ) required to produce the desired  $C_L$  of 0.3, 0.5, and 0.75 for the original tapered NACA 0009 hydrofoil. These angle of attacks were used as the reference angle of attacks for the optimization. Thus, the optimization presented in Section 4 are for fixed  $\alpha$ , where the desired  $C_L$  at each  $\alpha$  is achieved by optimizing the FFD control points and the twist design variables to minimize  $C_D$ .

Table 5: Angle of attack required to produce desired lift coefficient for the tapered NACA 0009 hydrofoil at  $Re = 1.0 \times 10^6$  and  $M = 0.05$ .

$C_L$	$\alpha$
0.3	$3.75^\circ$
0.5	$6.30^\circ$
0.75	$9.50^\circ$

The influence of the number of design variables will be studied in Section 4.1. For the results shown in Section 4.2 and after, a total of 210 design variables were used with 200 FFD control points (10 spanwise  $\times$  10 chordwise  $\times$  2 thickness) and 10 spanwise twist design variables.

## 4. Results

### 4.1. Effect of Number of Design Variables

Using the adjoint-based optimization algorithm, the effect of the number of design variables on the optimization is investigated in this section. Presented results are for optimization of a tapered NACA 0009 hydrofoil for a design  $C_L$  of 0.75, at  $Re = 1.0 \times 10^6$  and  $M = 0.05$ , using the problem setup shown in Section 3.5. Figure 5 depicts the FFD volume with the 18, 48, 200, and 720 FFD control points. It should be noted that only the FFD control points were varied, while the number of twist design variables remained fixed in each case. To be consistent, the twist design variables were fixed as 3 in this study, to match with the number of spanwise FFD control points in the 18 FFD control points case. The spanwise twist design variables are defined at the root, the mid-span and the tip of the foil. As explained earlier, the maximum number of design variables used in the previous high-fidelity gradient-free optimization studies are typically restricted to 15 or less, due to more than quadratic increase in computational cost with the increase in number of design variables [35]. For the SNOPT adjoint-based algorithm, however, the increase in CPU time with increase in number of design variables is approximately linear [35], and hence, a larger number of design variables can be used. A comparison of the total CPU time and optimized  $C_D$  values for the single-point optimization at  $C_L = 0.75$  for the different number of design variables are shown in Table 6. The CPU time mentioned in Table 6 is distributed over 192 processors (2.80 GHz Intel Xeon E5-2680V2) on the University of Michigan High performance Computing (HPC) flux cluster, operated by Advanced research Computing. The HPC flux cluster uses QDR Infiniband, which helps in better scaling of the parallel codes by reducing the latency period. As shown in Figure 6, the optimizations converged to similar geometries in terms of the twist and camber distribution, but with significant differences in the sectional  $C_p$  profile. While the difference in  $C_D$  values was only 0.7% between the case with 21 and 723 design variables, there were differences in the optimized geometry and pressure profile, as observed from Figure 6ii. As noted from Figure 6ii, finer control in the optimization problem is needed to achieve better optimized design. For the cases with 203 and 723 design variables, the optimal solutions are practically the same, except the region very close to the root section. The results in Figure 6 suggest that at least 203 design variables (200 FFD control points and 3 twist variables) are needed for a simple, unswept, tapered hydrofoil to get a properly converged optimal solution. As the complexity of the problem increases, such as, if the problem of interest is a marine propeller instead of a hydrofoil, significantly higher number of design variable will be required to parametrize the geometry. Thus, the capability to handle a large number of design variables will be very beneficial in case of the actual marine propellers.

Table 6: Comparison of the total CPU time (distributed over 192 processors (2.80 GHz Intel Xeon E5-2680V2), as the code is fully parallel) and  $C_D$  for the optimization problem for the different number of design variables at  $C_L = 0.75$ . All the results were obtained using RANS solver with  $Re = 1.0 \times 10^6$  and  $M = 0.05$ . The spanwise twist design variables are defined at the root, the mid-span and the tip of the foil.

Total Design Variables	FFD Control Points	Twist Variables	CPU time (in processor hours)	$C_D$
21	18	3	448	0.0396
51	48	3	638	0.0394
203	200	3	768	0.0393
723	720	3	1536	0.0393

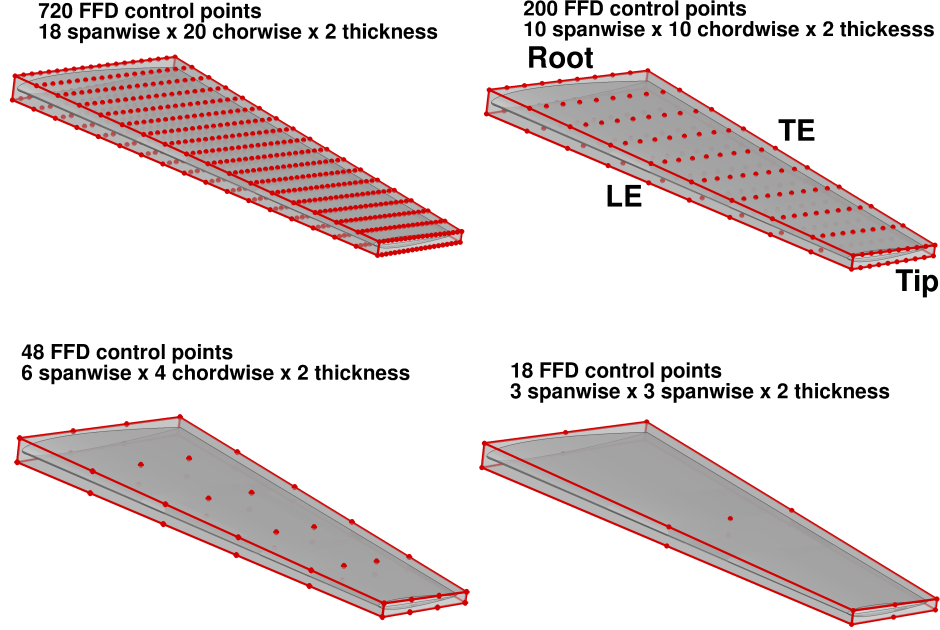


Figure 5: Figure depicting the different FFD volumes used to study the effect of number of FFD design variable on the RANS-based optimization. The circles denotes the FFD control points. Please note that the total number of design variables is equal to the number of FFD control points plus the three twist variables. The spanwise twist design variables are defined at the root, the mid-span and the tip of the foil, to be consistent with the 18 FFD control points case as shown in lower right hand corner.

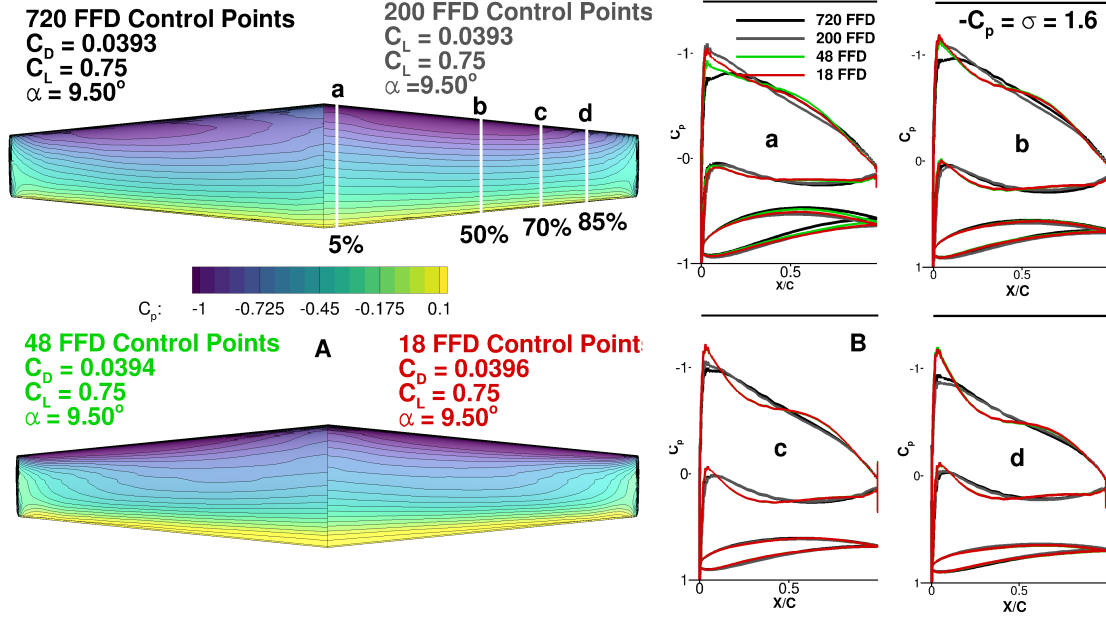
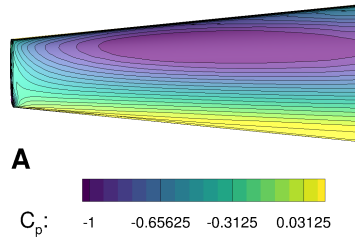


Figure 6: Figure depicting the single-point optimization results for tapered NACA 0009 hydrofoil at  $C_L = 0.75$ . Results show the difference in optimization with 18, 48, 200, and 720 FFD control points for a simple, unswept, hydrofoil at  $Re = 1.0 \times 10^6$  and  $M = 0.05$ . Please note that the total number of design variables include FFD control points and 3 spanwise twist design variables (defined at the root, the mid-span and the tip of the foil) in each case. The optimization problem specified was to minimize  $C_D$  for a given  $C_L$  of 0.75 and  $\sigma$  of 1.6. i) The difference in the  $C_D$  values was found to be very small, with the maximum difference in  $C_D$  values just less than 0.7%. ii) The optimization results converged to similar geometries (particularly in terms of the twist and camber distribution), but with significant differences in the sectional pressure profile noticed for the case with 18 FFD control points and 720 FFD control points. Black horizontal line represents the constraint on cavitation number. The optimized solution are practically the same for 200 and 720 FFD control points, except the region very close to the root section.

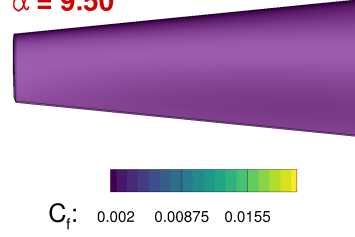
#### 4.2. Importance of Considering Viscous Effects

In this section, the advantage of using high-fidelity solver (RANS equations) over a lower fidelity solver (Euler equations), is demonstrated. The Euler solver used for this study is a purely inviscid solver, with no external correction for viscosity. For cases below stall and with low to moderate loading conditions, viscous effects are negligible, so the Euler-based and RANS-based optimization will lead to similar optimized geometry and performance. In this section, a high loading case ( $C_L = 0.75$ ) is presented to illustrate the need for the high-fidelity RANS solver at high  $C_L$  values, where impending stall and flow reversal make the effects of viscosity critical. Presented results are for optimization of a tapered NACA 0009 hydrofoil at  $Re = 1.0 \times 10^6$  and  $M = 0.05$ , using the problem setup, shown in Section 3.5. The optimization was carried out for  $C_L = 0.75$  using both the Euler and the RANS solver. The problem setup for both the Euler and the RANS optimization cases is the same, including geometry and mesh size, with the only difference being the flow solver. 210 shape design variables (200 FFD design variables and 10 spanwise twist variables) were used in both the cases. Figure 7 i)–iv) depicts the  $C_p$  contour plots on the left side and the skin friction coefficient ( $C_f$ ) contours on the right side for the Euler-based optimized foil for  $\alpha = 9.50^\circ$  and  $C_L = 0.75$ , the RANS analysis of the Euler-based optimized foil at  $\alpha = 9.50^\circ$  (which yield a  $C_L$  of 0.66), the RANS analysis of the Euler-based optimized foil at  $C_L = 0.75$  (which required an  $\alpha$  of  $10.51^\circ$ ), and the RANS-based optimized foil at  $C_L = 0.75$  and  $\alpha = 9.50^\circ$ . As observed from Figure 7, the predicted drag coefficient obtained from the Euler optimization at  $\alpha = 9.50^\circ$  is less than that from the RANS optimization, which is expected since the Euler solver assumes inviscid flow. When the RANS analysis was carried out on the Euler-optimized foil, the result was significantly different. At  $\alpha = 9.50^\circ$ , the RANS analysis show that Euler-based optimized foil only produces  $C_L$  of 0.66 and  $C_D$  of 0.0364. To obtain the desired  $C_L$  of 0.75, an  $\alpha$  of  $10.51^\circ$  is required for the Euler-based optimized foil, and the resultant  $C_D$  with RANS analysis of the Euler-optimized foil was 11.7% higher than the  $C_D$  from the RANS-based optimized foil. The above mentioned differences are due to viscous effects, which are not considered in an Euler solver. At  $\alpha = 9.50^\circ$ , significant differences in the sectional optimized geometry and the pressure profile, between the Euler-based optimized foil, the RANS-based optimized foil, and the RANS analysis of the Euler-optimized, can be noted from Figure 7v). The pressure distribution on the RANS-based optimized foil and the Euler-based optimized foil are significantly different because the different solvers result in different converged optimal geometries, as shown in Figure 7v). This demonstration clearly illustrates the need of high-fidelity solver to carry out hydrodynamic optimization at high  $C_L$  values, especially for the off-design points (where the flow might separate).

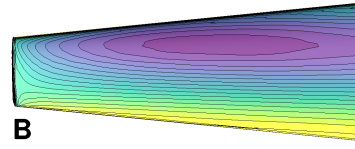
### Euler-based Optimized foil



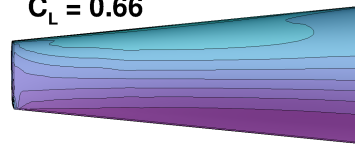
$C_D = 0.0270$   
 $C_L = 0.75$   
 $\alpha = 9.50^\circ$



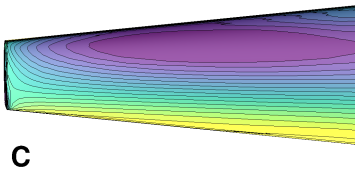
### RANS analysis of Euler-based Optimized foil at $\alpha = 9.50^\circ$



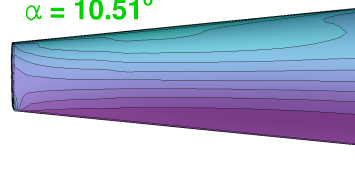
$C_D = 0.0364$   
 $C_L = 0.66$



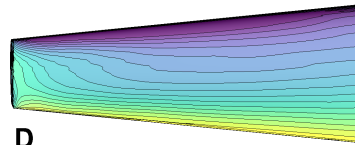
### RANS analysis of Euler-based Optimized foil at $C_L=0.75$



$C_D = 0.0439$   
 $\alpha = 10.51^\circ$



### RANS-based Optimized foil



$C_D = 0.0393$   
 $C_L = 0.75$   
 $\alpha = 9.50^\circ$

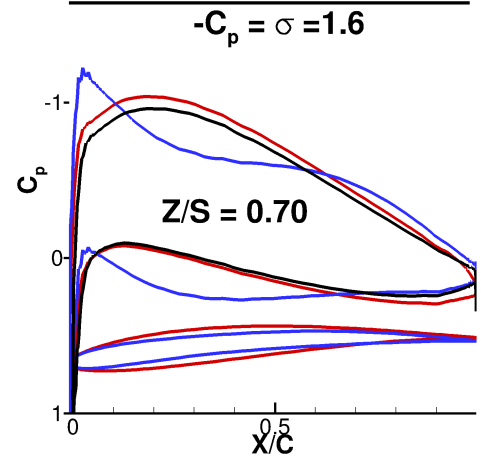
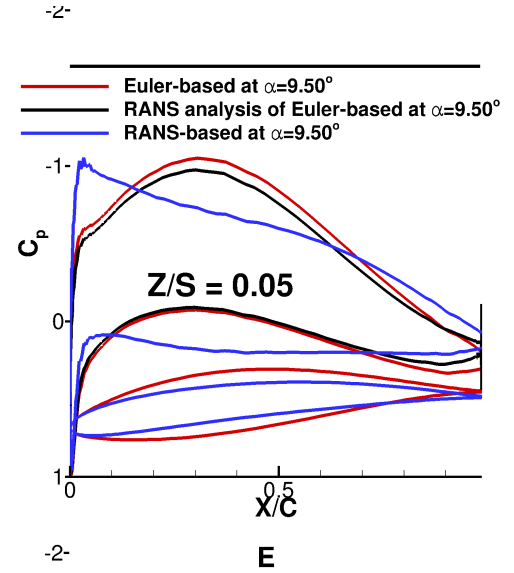
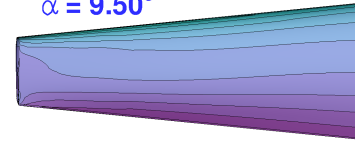


Figure 7: Figure showing the importance of high-fidelity solver in the design optimization tool. Optimization of the NACA 0009 hydrofoil at  $Re = 1.0 \times 10^6$  and  $M = 0.05$  for a given  $C_L$  of 0.75 was carried out using an Euler and a RANS solver. i)–iv)  $C_p$  contour plot on the suction side of the foil are displayed on the left side and the skin friction coefficient contour is plotted on the right side for the Euler-based optimized foil for  $\alpha = 9.50^\circ$  and  $C_L = 0.75$ , the RANS analysis of the Euler-based optimized foil at  $\alpha = 9.50^\circ$  (which yield a  $C_L$  of 0.66), the RANS analysis of the Euler-based optimized foil at  $C_L = 0.75$  (which required an  $\alpha$  of  $10.51^\circ$ ), and the RANS-based optimized foil at  $C_L = 0.75$  and  $\alpha = 9.50^\circ$ . Please note that the contour scale remains consistent for all the results. i) The predicted drag of the Euler-based optimized foil is less than the RANS-based optimized foil, as an Euler solver assumes inviscid flow. ii) At  $\alpha = 9.50^\circ$ , the RANS-analysis of Euler optimized foil produces  $C_L$  of 0.66 with  $C_D = 0.0364$ . This is due to the fact that Euler solver does not consider viscous effects. iii) To produce  $C_L = 0.75$ , the Euler-optimized foil will require an  $\alpha$  of  $10.51^\circ$  and the corresponding  $C_D$  is 0.0439, which is 11.7% higher than the RANS-optimized foil at  $C_L = 0.75$ . iv) RANS-optimized results for  $C_L = 0.75$  and  $\alpha = 9.50^\circ$ . v) Black horizontal line represents the constraint on cavitation number. Significant differences can be observed in the pressure profile and sectional geometry profile (at  $Z/S = 0.05$  and  $Z/S = 0.70$ ) between the Euler-based optimized foil, the RANS-based optimized foil, and the RANS-analysis of the Euler-based optimized foil, at  $\alpha = 9.50^\circ$ .

### 4.3. Single-Point Hydrodynamic Shape Optimization

In this section, the single-point RANS-based hydrodynamic design optimization results are presented for an unswept, tapered NACA 0009 hydrofoil at  $Re = 1.0 \times 10^6$  and  $M = 0.05$ . The foil was optimized to achieve the minimum drag coefficient ( $C_D$ ) for a target lift coefficient ( $C_L$ ) and a cavitation number ( $\sigma$ ) of 1.6. The optimization was carried out with 210 shape design variables (200 FFD design variables and 10 spanwise twist variables). Note that the NACA 0009 hydrofoil is already a very efficient hydrofoil to begin with, which makes the optimization problem more challenging. The single-point optimization took 790 processor hours (distributed over 192 processors, 2.80 GHz Intel Xeon E5-2680V2) on the University of Michigan HPC flux cluster.

To investigate how the optimal geometry changes with the design  $C_L$ , the single-point optimization were carried out for each  $C_L$ . To demonstrate the case at the highest design  $C_L$ , Figure 8 shows a detailed comparison of the tapered NACA 0009 hydrofoil and the optimized hydrofoil at a  $C_L$  of 0.75. As shown in Figure 8ii, the spanwise sectional lift distribution for the optimized foil is much closer to the ideal elliptical distribution. The gradient of the sectional lift distribution is also reduced near the tip region for the optimized foil, which translates to reduction in the strength of the tip vortex. The maximum negative pressure coefficient,  $-C_p$ , reduces from 3.1 for the NACA 0009 hydrofoil to 1.2 for the optimized foil, as shown in Figure 8iii, which will help to significantly delay cavitation inception. In order words, cavitation inception speed for the optimized foil will increase from 8.4 m/s to 13.50 m/s, for an assumed submergence depth of 1 m. The results indicate that partial leading edge cavitation (as indicated by the white contour region with  $-C_p \geq \sigma$ ) will develop around the original NACA 0009 hydrofoil at  $C_L = 0.75$  and  $\sigma = 1.6$ , but no cavitation is observed for the optimized foil. As observed from Figure 8iii, the optimized foil has a higher camber and a non-zero spanwise twist/pitch distribution compared to the original NACA 0009 hydrofoil, which reduced the effective angle of attack and shifted the loading more towards the mid-chord of the foil.

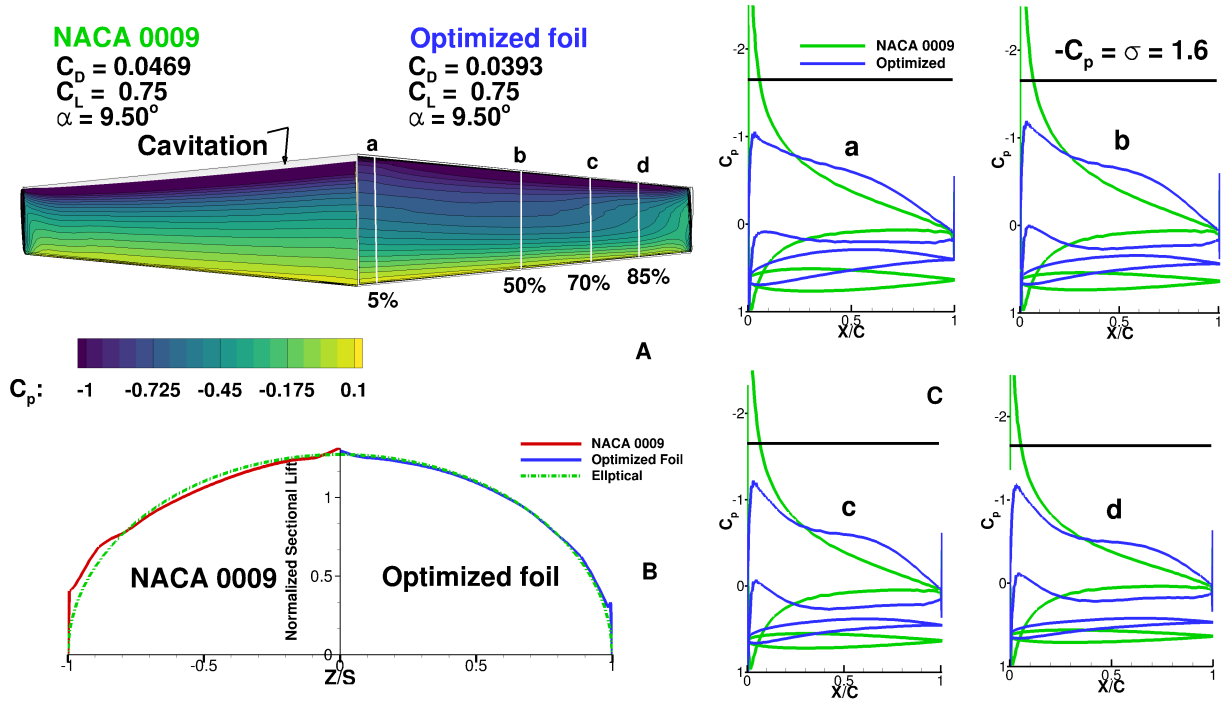


Figure 8: Figure showing single-point optimization result for a tapered NACA 0009 hydrofoil at  $C_L = 0.75$ ,  $Re = 1.0 \times 10^6$ , and  $M = 0.05$ . A reduction in  $C_D$  of 14.4% is noted for the optimized foil. Going from top to bottom and from left to right. i)  $C_p$  (pressure coefficient) contours plot on the suction side are displayed for NACA 0009 hydrofoil and the optimized foil. White lines along the span of the hydrofoil show the section where the  $-C_p$  plots and sectional geometry are compared in the plots shown on the right. White contour region along the leading edge of the tapered NACA 0009 foil shows the area with  $-C_p \geq \sigma$ . ii) Comparative study of the normalized sectional lift distribution with the ideal elliptical lift distribution for the original foil (on the left side) and for the optimized foil (on the right side). There is reduction in the gradient at the tip region for the optimized foil, which also results in reduced tip vortex strength. iii) Figures show the sectional  $-C_p$  plots and the geometry profile of the foil at 4 sections along the span of the hydrofoil, the section locations are define in i). Grey solid line represents the NACA 0009 hydrofoil and the black solid line corresponds to the optimized foil. Black horizontal line represents the constraint on cavitation number. As noted, there is significant decrease in maximum  $-C_p$  from the NACA 0009 to the optimized hydrofoil. Difference in the sectional shape between the original and optimized foil are also shown in the bottom of each subplot.

Figure 9 shows the comparison of efficiency (i.e.  $C_L/C_D$ ) at the various design  $C_L$  values for the NACA 0009 hydrofoil, the single-point optimized foil at each  $C_L$  value, and the single-point optimized foil at  $C_L = 0.75$  only. It should be noted that the single-point optimized foil at each  $C_L$  requires a different geometry at each  $C_L$  (as shown in Figure 10), thus it can only be achieved if there is a robust active morphing capability. Assuming that there is an active morphing capability, with the single-point optimization at each  $C_L$  value, the best possible performance is achieved; there is a minimum increase in efficiency of 6.4% throughout the operating regime, and the increase in efficiency is 19% at the  $C_L$  value of 0.75, over the original NACA 009 hydrofoil. With the single-point optimized foil at  $C_L = 0.75$



only, due to fixed geometry; degraded performance was noted when operating away from  $C_L = 0.75$ ; in particular, at  $C_L = 0.3$ , the single-point optimized foil for  $C_L = 0.75$  only resulted in a higher  $C_D$  value than the original NACA 0009 hydrofoil. Thus, the results show that, unless there is a robust active morphing capability available, there is a need for the multipoint optimization to achieve a globally optimal design using one fixed geometry, as demonstrated next in Section 4.4.

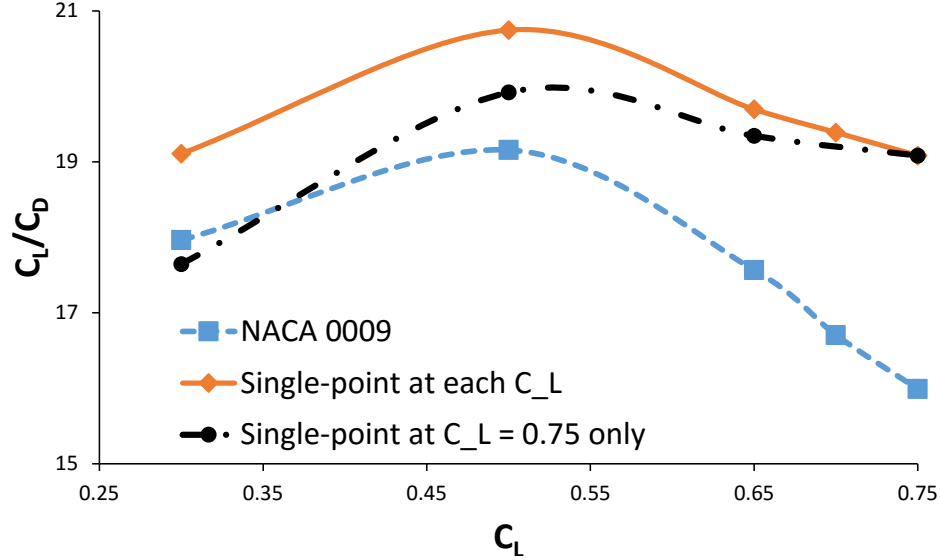


Figure 9: Figure showing the comparison of efficiency (i.e.  $C_L/C_D$ ) versus  $C_L$  for the tapered NACA 0009 hydrofoil with the single-point optimized foil at each  $C_L$ , and the single-point optimized foil at  $C_L = 0.75$  only. All the results were obtained using RANS solver with  $Re = 1.0 \times 10^6$  and  $M = 0.05$ .

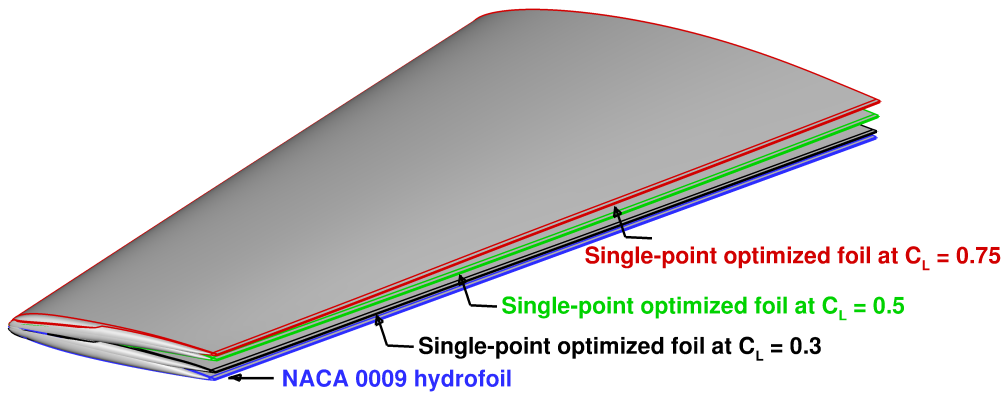


Figure 10: Figure showing the comparison of 3-D geometry between the original tapered NACA 0009 foil, the single-point optimized foil at  $C_L = 0.30$ , the single-point optimized foil at  $C_L = 0.50$ , and the single-point optimized foil at  $C_L = 0.75$ . The RANS-based optimization were carried out at  $Re = 1.0 \times 10^6$  and  $M = 0.05$ .

#### 4.4. Comparison of multipoint Optimization and Single-point Optimization

As shown in Section 4.3, the single-point optimization does not necessary result in a globally optimal solution with the best efficiency possible over the entire range of operating conditions. The design optimized for  $C_L = 0.75$  lead to a higher  $C_D$  than the original foil at  $C_L = 0.3$ . Such a design would lead to low overall efficiency, particularly if the probability of operating at  $C_L = 0.75$  is low. Hence, a probabilistic multipoint optimization study is needed.

For the probabilistic multipoint optimization problem, the objective function ( $\Pi_{obj}$ ) is adapted as,

$$\Pi_{obj} = \sum_{m=1}^K C_{Dm} P_m \quad (15)$$

where  $C_{Dm}$  is the drag coefficient at point  $m$ ;  $P_m$  is the probability of operating at point  $m$ ; and  $K$  is the number of design  $C_L$  points.

To compare the difference between a single-point and a probabilistic multipoint optimization, a simple three point probability distribution, as shown in Table 7, was chosen. The objective function is to minimize the sum of the drag coefficient at the three target  $C_L$  values weighted by the probability of operating at the particular  $C_L$  value, as shown in Eq. 15. The cavitation number ( $\sigma$ ) was fixed at 1.6. The problem setup remains same as shown in Section 3.5. However, to make sure that the problem is well-posed, the angle of attack (define with respect to the original undeformed FFD volume) for  $C_L = 0.75$  was fixed at  $9.50^\circ$ , and the angle of attacks for the other  $C_L$  values in the multipoint problem are allowed to be design variables. The multipoint optimization took 2410 processor hours (distributed over 192 processors, 2.60 GHz Intel Xeon E5-2680V2) on the University of Michigan HPC flux cluster.

Table 7: The simple probabilistic multipoint profile used in the current example.

$C_L$	Weights/Probability
0.30	0.15
0.50	0.25
0.75	0.60

Figure 11 shows the comparison of 3-D geometry between the original NACA 0009 hydrofoil, the single-point optimized foil at  $C_L = 0.75$ , and the probabilistic multipoint optimized foil. Significant difference is observed in the twist/pitch distribution and in the camber distribution for the three foil geometries.

The bar-chart in Figure 12 shows a comparison of the  $C_D$  values for the original NACA 0009 hydrofoil, the single-point optimized foil at  $C_L = 0.75$ , the multipoint optimized foil, and the single-point optimized foil at each  $C_L$  value (which indicates the hypothetical best performance scenarios with active morphing capability, as explained in Section 4.3). All the results were obtained using the RANS solver. The line in the plot depicts the probability distribution (as shown in Table 7) used for the multipoint design. As expected, the single-point design for  $C_L = 0.75$  performed the best at  $C_L = 0.75$ ; the multi-point design showed the next best performance at  $C_L = 0.75$ , with only 1.4% reduction in efficiency compared to the single-point optimized design at  $C_L = 0.75$ . Notice that while the performance of single-point optimized foil for  $C_L = 0.75$  only is even worse than the original tapered NACA 0009 hydrofoil for  $C_L = 0.3$ , the probabilistic multipoint design performs better than the original NACA 0009 hydrofoil for all  $C_L$  values.

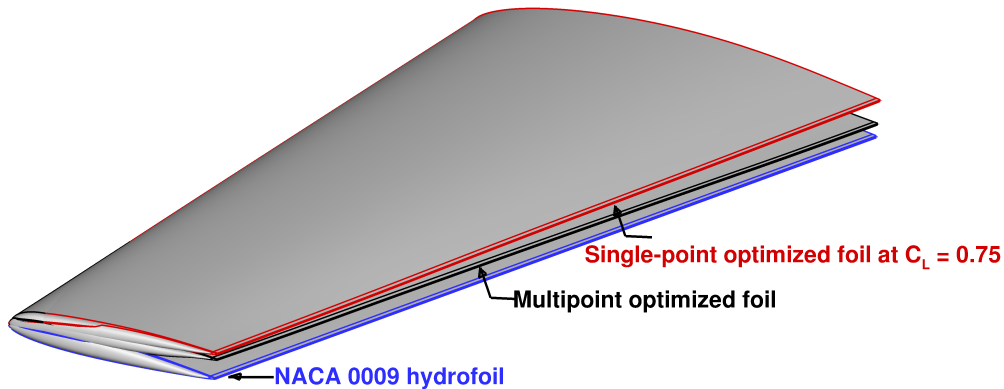


Figure 11: Figure showing comparison of the 3-D geometry between the original tapered NACA 0009, probabilistic multipoint optimized foil and the single-point optimized foil at  $C_L = 0.75$ . All the simulations were carried out using the RANS solver, with  $Re = 1.0 \times 10^6$  and  $M = 0.05$ .

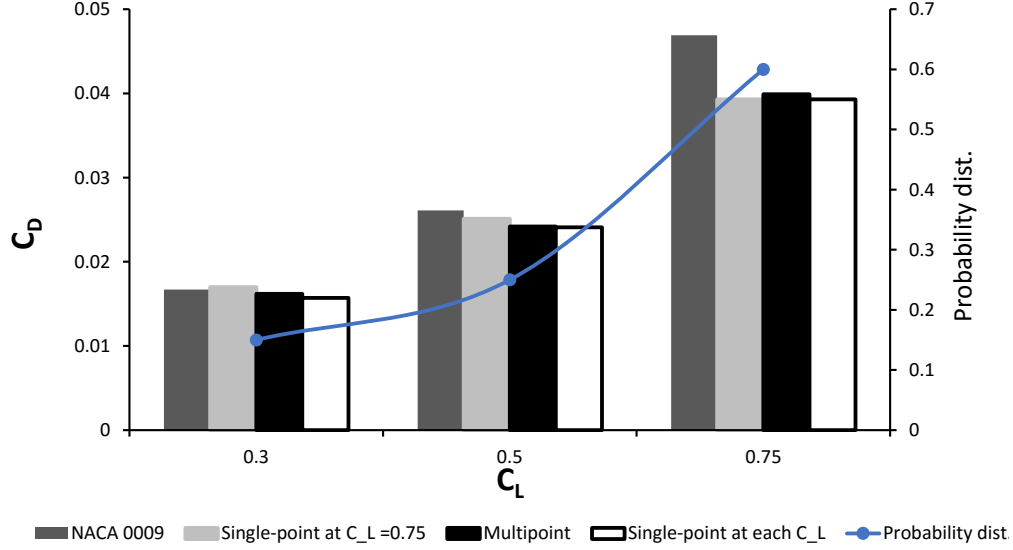


Figure 12: The comparison of  $C_D$  at different  $C_L$  values of 0.3, 0.5, and 0.75 for the original tapered NACA 0009 hydrofoil, single-point optimized foil at  $C_L = 0.75$  only, probabilistic multipoint optimized foil with fixed geometry, and single-point optimized foil at each  $C_L$ , with varying geometry at each  $C_L$ . All the results are obtained using the RANS solver with  $Re = 1.0 \times 10^6$  and  $M = 0.05$ . The line depicts the probability distribution (as shown in Table 7) used for the multipoint optimization problem.

A comparison of the detailed performance of the original tapered NACA 0009 hydrofoil, the single-point optimization at  $C_L = 0.75$ , and the probabilistic multipoint optimization is shown in Figure 13. Columns 2–4 in Figure 13 shows the predicted  $C_p$  contours for the foils at the  $C_L$  values specified in the first column. The last column in Figure 13 shows the difference in geometry for the original NACA 0009 hydrofoil, the single-point optimized foil, and the multipoint optimized foil at  $Z/S = 0.5$ . The maximum negative pressure coefficient,  $-C_p$ , reduces from 2.9 and 3.1 for the NACA 0009 hydrofoil to 1.3 and 1.5 for the multipoint optimized foil, at  $C_L = 0.5$  and  $C_L = 0.75$ , respectively. As noted from Figure 13 Column 2–4, partial leading edge cavitation will develop around the NACA 0009 hydrofoil for  $C_L \geq 0.5$  and  $\sigma = 1.6$ , but no cavitation is observed for both the optimized foils (the single-point optimized foil and the multipoint optimized foil). Notice that the single-point optimized foil at  $C_L=0.75$  has a much higher camber and a more negative pitch/twist compared to the original foil and the multipoint design; hence the single-point optimized foil at  $C_L = 0.75$  behaves poorly at the lower  $C_L$  values. As  $C_L = 0.75$  has the highest probability/weight in the probabilistic multipoint optimization, the performance of the multipoint optimized foil and single-point optimized foil at design  $C_L$  of 0.75 is almost same with respect to  $C_D$  values. However, at other  $C_L$  points in the multipoint optimization, the multipoint design showed better performance, which is expected.

The results show, while the single-point optimization can achieve the best efficiency at the design  $C_L$ , the single-point optimized foil showed reduced performance at the off-design conditions, namely,  $C_L = 0.3$  and  $C_L = 0.5$ . If the overall efficiency is calculated as the sum of the efficiency at each  $C_L$  value multiplied by the probability of operating at each  $C_L$ , the probabilistic multipoint optimized foil will result in overall increase in the efficiency by around 14.4% over the original NACA 0009 hydrofoil. It should be noted that the overall efficiency of the multipoint design (with a fixed geometry) is only 1.5% less than the best possible solution from the hypothetical morphing foil (i.e. with varying geometry at each  $C_L$ ). The increase in the cavitation inception speed compared to the original NACA 0009 foil, is 49% at  $C_L = 0.50$ , and 39% at  $C_L = 0.75$ , for an assumed submergence depth of 1 m. This improvement in overall efficiency would be even more obvious if the probability of operating at the highest  $C_L$  is lower, which is often the case for many marine propulsors as they seldom operate at the highest loading condition. Thus, it is necessary to carry out the probabilistic multipoint optimization, using realistic mission/operation profiles at an intermediate design stage to achieve a design that performs well throughout the entire range of operating conditions.

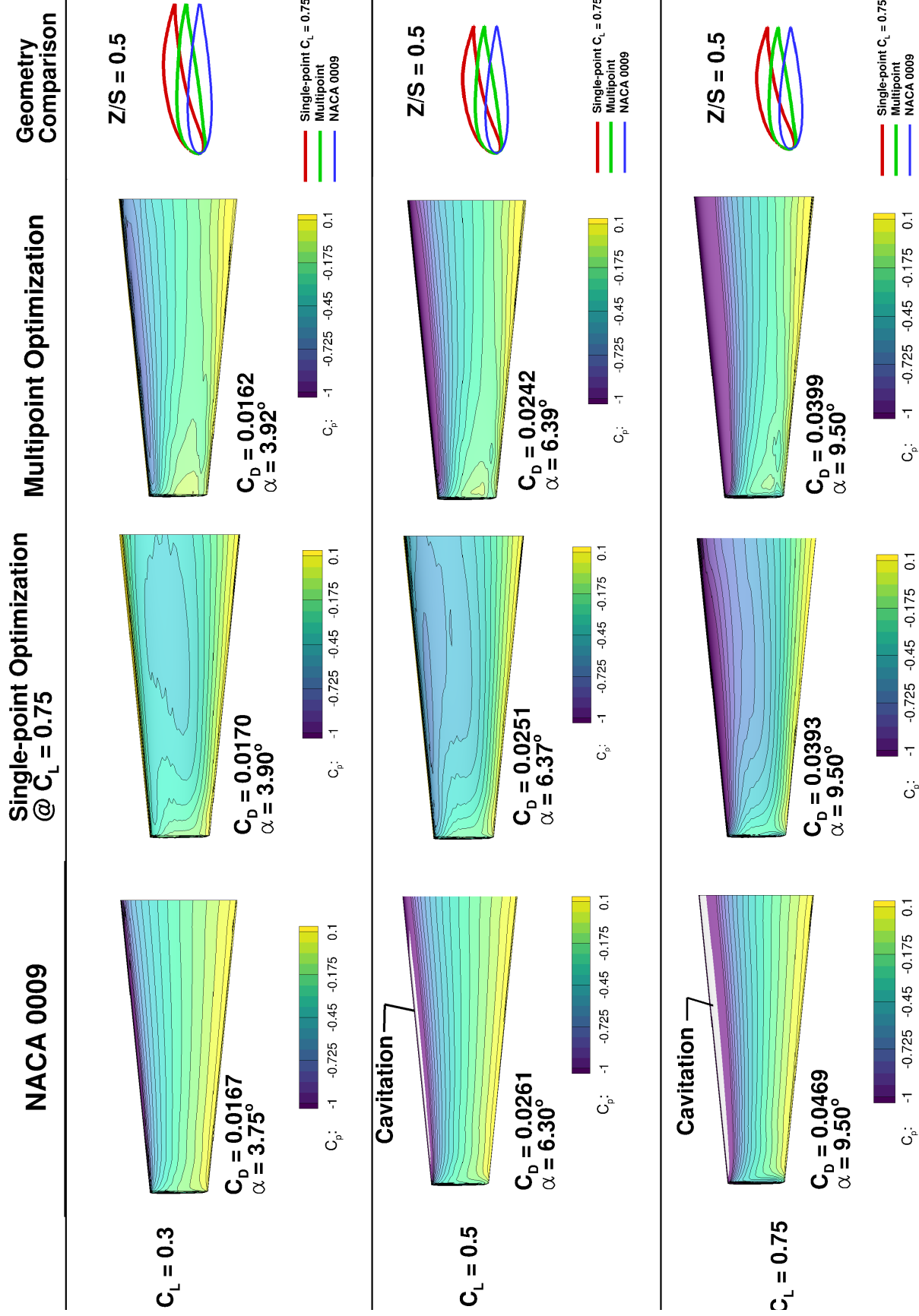


Figure 13: Figure showing the comparison of the original NACA 0009 hydrofoil, the single-point optimized foil at  $C_L = 0.75$ , and multipoint optimized foil. All the results are obtained using the RANS solver with  $Re = 1.0 \times 10^6$  and  $M = 0.05$ . Columns 2–4 shows the predicted  $C_p$  contours for the foils at the  $C_L$  values specified in the first column. The last column shows the difference in geometry for the original NACA 0009 hydrofoil, the single-point optimized foil and the multipoint optimized foil at  $Z/S = 0.5$ . Notice the white contour region along the leading edge for the original NACA 0009 hydrofoil indicates the region with  $-C_p \geq \sigma$ . Note that the figures in the last column are not plotted to scale, to show the difference in geometries more prominently. It can be observed from the  $C_D$  values that while the single-point optimized foil only performs well at the optimized point and performs poorly at the off-design point, while the probabilistic multipoint optimized design performs over the entire range of operating conditions.

## 5. Conclusions

In the present work, a low-speed (LS) preconditioner was implemented in an existing compressible CFD solver, SUMad, to solve problems involving nearly incompressible flows for Mach numbers as low as 0.01. The LS SUMad RANS solver was validated against experimental data [25] and verified against commercial CFD software results for the case of a tapered stainless steel NACA 0009 hydrofoil. The LS SUMad, over predicts the  $C_D$  values by 14.37% and  $C_L$  values are under-predicted by 3.3%, when compared with experimental results [25]. However, when LS SUMad results were compared with commercial CFD software (ANSYS CFX), the average difference was 2.9% in  $C_L$  and 1.7% in  $C_D$  values, inspite of the different turbulent models.

A design constraint on the cavitation number was developed to optimize the foil to avoid or delay cavitation. The development of this cavitation constraint coupled with the adjoint-based optimization algorithm resulted in an efficient and high-fidelity hydrodynamic shape optimization tool for the 3-D lifting surfaces operating under water. To provide a canonical representation of a general hydrodynamic lifting surface, the RANS-based optimization results using the adjoint method were presented for an unswept, tapered NACA 0009 hydrofoil at  $Re = 1.0 \times 10^6$  and  $M = 0.05$ .

The effect of the number of shape design variables was studied in detail. It was found that while the change in  $C_D$  values was not significant, the pressure distribution and geometry varied significantly with the number of shape design variables. For the hydrofoil considered in this study, a minimum of 203 design variables (200 FFD control points and 3 twist variables) was needed to achieve an acceptable optimal solution.

The need for RANS-based design optimization as opposed to Euler-based design optimization was demonstrated. This was evidenced by the fact that 1) the RANS-based and Euler-based design optimizations for the same  $C_L$  lead to significantly different geometry, and 2) the RANS analysis of the Euler-based optimized foil showed that it cannot deliver the required lift unless the angle of attack is increased; moreover, to deliver the same  $C_L$ , RANS-analysis of the Euler-based optimized foil will lead to a 11.7% higher drag coefficient, compared to the RANS-optimized foil.

To demonstrate the power of the RANS-based shape optimization methodology, a series of optimizations were performed for the tapered hydrofoil. A single-point optimization was conducted at each  $C_L$  value with 210 design variables, where the optimized geometry was significantly different for each  $C_L$ , and hence a robust active morphing method would be needed to realize this design. Nevertheless, such an actively morphed foil would lead to at least an increase in efficiency of 6.4% throughout the operating profile, and the increase in efficiency would increase to 19% for  $C_L = 0.75$ . The optimized foil at  $C_L = 0.75$ , would also lead to an increase in the cavitation inception speed by 60%, compared to the original NACA 0009 hydrofoil. However, performance of single-point optimized foil degraded when operated away from the design  $C_L$  value. In particular, the foil optimized for the highest lift coefficient ( $C_L = 0.75$ ) showed inferior performance even when compared to the original foil at the lowest lift coefficient ( $C_L = 0.3$ ) condition.

To overcome the issue of degraded performance of the single-point optimized design at the off-design conditions, a multipoint optimization was carried out. The multipoint optimization was found to perform better than the original NACA 0009 hydrofoil over the entire operation profile, where the overall efficiency weighted by the probability of operation at each  $C_L$ , was improved by 14.4% compared to the original NACA 0009 foil. The increase in the cavitation inception speed compared to the original NACA 0009 foil, was 49% at  $C_L = 0.50$  and 39% at  $C_L = 0.75$ , for an assumed submergence depth of 1 m. For the multipoint optimized foil, the geometry remains fixed through out the operation range and the overall efficiency was only 1.5% less than the hypothetical actively morphed foil with the optimal geometry at each  $C_L$ . The results show that the proposed high-fidelity optimization tool can be used to carry out the probabilistic multipoint optimization, using realistic operation profiles at an intermediate design stage to achieve a design that performs well throughout the entire range of operating conditions.

Thus, a thorough study of the design space of marine propulsors using the presented high-fidelity multipoint optimization methodology has the potential to dramatically improve fuel efficiency, agility, and performance over a wide range of operating conditions, including extreme off-design conditions (such as crash-stop maneuvers, hard turns, and maneuvering), while at the same time delaying cavitation inception.

## 6. Future work

The purpose of this paper is to introduce an efficient high-fidelity hydrodynamic shape design optimization tool, capable of handling a large number of design variables over a wide range of operating conditions. In this paper, a tapered NACA 0009 hydrofoil is presented as a canonical representation of more complex geometries such as marine propellers. The capability of handling large number of design variables should be highly beneficial when designing

much more complex geometries and different material configurations, such as those of composite marine propellers and hulls. An efficient high-fidelity solver will also give the freedom to carry out probabilistic multipoint optimization studies. Such high-fidelity tool is needed at extreme off-design conditions (e.g., crash-stop maneuvers), where the solution is governed by separated flow and the large scale vortices. Using the current tool, the optimal design over the entire range of operating conditions can help designers to achieve the ever increasing minimum energy efficiency level per capacity mile, as required by Energy Efficiency Design Index (EEDI), and also to reduce the operating costs of the marine vessels. Future work should also include hydrostructural optimization, which would optimize not only the shape, but also the material configuration of the marine propulsors, hydrofoils or hulls, similarly to what has already been done for aircraft wings [39, 40, 27]. With hydrostructural design optimization, designer can control and tailor the fluid structure interaction response and reduce the structural weight while ensuring structural integrity. Potential examples where hydrostructural optimization can be critical include composite propulsors and turbines, where the load-dependent transformations can be tailored to reduce dynamic load variations, delay cavitation inception, and improve fuel efficiency by adjusting the blade or foil shape in off-design conditions or in spatially varying flow [41, 42].

## Acknowledgements

The computations were performed on the Flux HPC cluster at the University of Michigan Center of Advanced Computing.

Support for this research was provided by the U.S. Office of Naval Research (Contract N00014-13-1-0763), managed by Ms. Kelly Cooper.

## References

- [1] J. E. Kerwin, Marine propellers, *Annual review of fluid mechanics* 18 (1) (1986) 367–403.
- [2] C. Y. Hsin, Application of the panel method to the design of two-dimensional foil sections, *Journal of Chinese society of Naval Architects and Marine Engineers* 13 (1994) 1–11.
- [3] C. Y. Hsin, J. L. Wu, S. F. Chang, Design and optimization method for a two-dimensional hydrofoil, *Journal of Hydrodynamics* 18(3) (2006) 323–329.
- [4] J. Cho, S.-C. Lee, Propeller blade shape optimization for efficiency improvement, *Computers & fluids* 27 (3) (1998) 407–419.
- [5] W. Wilson, J. Gorski, M. Kandasamy, H. Takai, T. F. W., Stern, Y. Tahara, Hydrodynamic shape optimization for naval vehicles, *High Performance Computing Modernization Program Users Group Conference (HPCMP-UGC)* (2010) 161–168.
- [6] E. Campana, D. Peri, Y. Tahara, M. Kandasamy, F. Stern, C. Cary, R. Hoffman, J. Gorski, C. Kennell, Simulation-based design of fast multihull ships, *26th Symposium on Naval Hydrodynamics*, September 17–22.
- [7] A. Jameson, Computational aerodynamics for aircraft design, *Science* 245 (1989) 361–371.
- [8] W. K. Anderson, V. Venkatakrishnan, Aerodynamic design optimization on unstructured grids with a continuous adjoint formulation, *Computers and Fluids* 28 (4) (1999) 443–480.
- [9] J. J. Reuther, A. Jameson, J. J. Alonso, M. J. Rimlinger, D. Saunders, Constrained multipoint aerodynamic shape optimization using an adjoint formulation and parallel computers, part 1, *Journal of Aircraft* 36 (1) (1999) 51–60.
- [10] J. J. Reuther, A. Jameson, J. J. Alonso, M. J. Rimlinger, D. Saunders, Constrained multipoint aerodynamic shape optimization using an adjoint formulation and parallel computers, part 2, *Journal of Aircraft* 36 (1) (1999) 61–74.
- [11] J. E. V. Peter, R. P. Dwight, Numerical sensitivity analysis for aerodynamic optimization: A survey of approaches, *Computers and Fluids* 39 (2010) 373–391. doi:10.1016/j.compfluid.2009.09.013.
- [12] Z. Lyu, G. K. Kenway, J. R. R. A. Martins, Aerodynamic shape optimization studies on the Common Research Model wing benchmark, *AIAA Journal* 53 (4) (2015) 968–985. doi:10.2514/1.J053318.

- [13] M. R. Motley, M. Nelson, Y. L. Young, Integrated probabilistic design of marine propulsors to minimize lifetime fuel consumption, *Ocean Engineering* 45 (2012) 1–8.
- [14] M. R. Kramer, M. R. Motley, Y. L. Young, An integrated probability-based propulsor-hull matching methodology, *Journal of Offshore Mechanics and Arctic Engineering* 135 (1) (2013) 011801.
- [15] M. Nelson, D. W. Temple, J. T. Hwang, Y. L. Young, J. R. R. A. Martins, M. Collette, Simultaneous optimization of propeller–hull systems to minimize lifetime fuel consumption, *Applied Ocean Research* 43 (2013) 46–52.
- 570 [16] Y. L. Young, J. W. Baker, M. R. Motley, Reliability-based design and optimization of adaptive marine structures, *Composite structures* 92 (2) (2010) 244–253.
- [17] M. R. Motley, Y. L. Young, Performance-based design and analysis of flexible composite propulsors, *Journal of Fluids and Structures* 27 (8) (2011) 1310–1325.
- [18] T. Brockett, Minimum pressure envelopes for modified NACA-66 sections with NACA A= 0.8 camber and buships type 1 and type 2 sections, DTIC Document (1996).
- [19] R. Eppler, Y. T. Shen, Wing sections for hydrofoils–Part 1: Symmetrical profiles, *Journal of ship research* (1979) 23 (3).
- [20] Y. T. Shen, R. Eppler, Wing sections for hydrofoils–Part 2: Nonsymmetrical profiles, *Journal of ship research* 25 (3) (1981) 191–200.
- 580 [21] S. Kinnas, S. Mishima, W. Brewer, Nonlinear analysis of viscous flow around cavitating hydrofoils, in: 20th Symposium on Naval Hydrodynamics, 1994, pp. 21–26.
- [22] S. Mishima, S. A. Kinnas, A numerical optimization technique applied to the design of two-dimensional cavitating hydrofoil sections, *Journal of Ship Research* 40(1) (1996) 28–38.
- [23] Non-linear analysis of the flow around partially or super-cavitating hydrofoils by a potential based panel method.
- [24] Z. B. ZENG, G. Kuiper, Blade section design of marine propellers with maximum cavitation inception speed, *Journal of Hydrodynamics* 24(1) (2011) 65–75.
- [25] Z. G.A., P. Brandner, B. Pearce, A. W. Phillips, Experimental study of the steady fluid-structure interaction of flexible hydrofoils, *Journal of Fluids and Structure* 51 (2014) 326–343.
- 590 [26] G. K. W. Kenway, G. J. Kennedy, J. R. R. A. Martins, Scalable parallel approach for high-fidelity steady-state aeroelastic analysis and derivative computations, *AIAA Journal* 52 (5) (2014) 935–951. doi:10.2514/1.J052255.
- [27] G. K. W. Kenway, J. R. R. A. Martins, Multipoint high-fidelity aerostructural optimization of a transport aircraft configuration, *Journal of Aircraft* 51 (1) (2014) 144–160. doi:10.2514/1.C032150.
- [28] E. van der Weide, G. Kalitzin, J. Schluter, J. J. Alonso, Unsteady turbomachinery computations using massively parallel platforms, in: Proceedings of the 44th AIAA Aerospace Sciences Meeting and Exhibit, Reno, NV, 2006, AIAA 2006-0421.
- [29] Z. Lyu, G. K. Kenway, C. Paige, J. R. R. A. Martins, Automatic differentiation adjoint of the Reynolds-averaged Navier–Stokes equations with a turbulence model, in: 21st AIAA Computational Fluid Dynamics Conference, San Diego, CA, 2013. doi:10.2514/6.2013-2581.
- 600 [30] A. Jameson, W. Schmidt, E. Turkel, Numerical solutions of the euler equations by finite volume methods using Runge–Kutta time-stepping schemes, *AIAA paper* (1981) 1259.
- [31] P. Spalart, S. Allmaras, A one-equation turbulence model for aerodynamic flows, in: 30th Aerospace Sciences Meeting and Exhibit, 1992. doi:10.2514/6.1992-439. URL <http://dx.doi.org/10.2514/6.1992-439>

- [32] E. Turkel, R. Radespiel, N. Kroll, Assessment of preconditioning methods for multidimensional aerodynamics, *Computer and Fluids* 26(6) (1997) 613–634.
- [33] Y. H. Choi, C. L. Merkle, The application of preconditioning in viscous flows, *Journal of Computational Physics* 105(2) (1993) 207–223.
- [34] B. Van Leer, W. T. Lee, P. L. Roe, Characteristic time-stepping or local preconditioning of the euler equations, 10th Computational Fluid Dynamics Conference 1 (1991) 260–282.
- [35] Z. Lyu, Z. Xu, J. R. R. A. Martins, Benchmarking optimization algorithms for wing aerodynamic design optimization, in: 8th International Conference on Computational Fluid Dynamics (ICCFD8), Chengdu, China, 2014, ICCFD8 2014-0203.
- [36] J. R. R. A. Martins, P. Sturdza, J. J. Alonso, The complex-step derivative approximation, *ACM Transactions on Mathematical Software (TOMS)* 29(3) (2003) 245–262.
- [37] J. R. R. A. Martins, J. T. Hwang, Review and unification of methods for computing derivatives of multidisciplinary computational models, *AIAA Journal* 51 (11) (2013) 2582–2599. doi:10.2514/1.J052184.
- [38] P. E. Gill, W. Murray, M. A. Saunders, SNOPT: An SQP algorithm for large-scale constrained optimization, *SIAM Journal on optimization* (2002) 976–1006.
- [39] G. K. W. Kenway, J. R. R. A. Martins, Multipoint aerodynamic shape optimization investigations of the Common Research Model wing, in: Proceedings of the AIAA Science and Technology Forum and Exposition (SciTech), Kissimmee, FL, 2015, aIAA 2015-0264. doi:10.2514/6.2015-0264.
- [40] R. Liem, G. K. W. Kenway, J. R. R. A. Martins, Multimission aircraft fuel burn minimization via multipoint aerostructural optimization, *AIAA Journal* 53 (1) (2015) 104–122. doi:10.2514/1.J052940.
- [41] Y. L. Young, Fluid–structure interaction analysis of flexible composite marine propellers, *Journal of Fluids and Structures* 24 (6) (2008) 799–818.
- [42] Y. L. Young, M. R. Motley, R. W. Yeung, Three-dimensional numerical modeling of the transient fluid-structural interaction response of tidal turbines, *Journal of Offshore Mechanics and Arctic Engineering* 132 (1) (2010) 011101.